# Investigations Regarding the Addition of ZnO and Li2O-TiO2 to Phosphate-Tellurite Glasses: Structural, Chemical, and Mechanical Properties

**Mihail Elisa** [1], **Stefan-Marian Iordache** [1,*], **Ana-Maria Iordache** [1], **Constantina Raluca Stefan** [1], **Ileana Cristina Vasiliu** [1], **Daniel Cristea** [2,*], **Doru Ursutiu** [3,4], **Cornel Samoila** [2,5], **Bogdan Alexandru Sava** [6,7,*], **Lucica Boroica** [6], **Marius Catalin Dinca** [6], **Ana Violeta Filip** [6], **Mihai Eftimie** [7] and **Monica Enculescu** [8]

[1] Optospintronics Department, National Institute of R & D for Optoelectronics INOE 2000, 077125 Magurele, Romania; elisa@inoe.ro (M.E.); ana.iordache@inoe.ro (A.-M.I.); raluca.iordanescu@gmail.com (C.R.S.); icvasiliu@inoe.ro (I.C.V.)

[2] Materials Science and Engineering Faculty, Transilvania University of Brasov, 500036 Brasov, Romania; csam@unitbv.ro

[3] Electrical Engineering and Computer Science Faculty, Transilvania University of Brasov, 500036 Brasov, Romania; udoru@unitbv.ro

[4] Academy of Romanian Scientists, 050044 Bucharest, Romania

[5] Technical Sciences Academy of Romania, 030167 Bucharest, Romania

[6] Laser Department, National Institute for Lasers, Plasma and Radiation Physics, 077125 Magurele, Romania; boroica_lucica@yahoo.com (L.B.); catalin69@live.com (M.C.D.); ana.filip@inflpr.ro (A.V.F.)

[7] Faculty of Applied Chemistry and Materials Science, Politehnica University of Bucharest, 060042 Bucharest, Romania; mihai.eftimie@upb.ro

[8] Multifunctional Materials and Structures Laboratory, National Institute of Materials Physics, 077125 Magurele, Romania; mdatcu@infim.ro

* Correspondence: stefan.iordache@inoe.ro (S.-M.I.); daniel.cristea@unitbv.ro (D.C.); bogdan.sava@inflpr.ro (B.A.S.)

**Abstract:** Phosphate and tellurite glasses can be used in optics, optoelectronics, magneto-optics, and nuclear and medical fields. Two series of phosphate-tellurite glasses, $(50-x)ZnO-10Al_2O_3-40P_2O_5-xTeO_2$ and $(40-x)Li_2O-10Al_2O_3-5TiO_2-45P_2O_5-xTeO_2$ ($x = 5, 10$), were synthesized by a non-conventional wet-route, and the mechanical properties as key performance measures for their application in optoelectronics were investigated. X-ray Diffraction (XRD) measurements revealed the vitreous nature of the investigated materials. Instrumented indentation tests allowed the calculation of hardness ($H$) and Young's modulus ($E$) using the Oliver and Pharr model. The influence of increasing the $TeO_2$ content, as well as the substitution of ZnO by $Li_2O-TiO_2$, on the variation of hardness, Young's modulus, penetration depth ($PD$), and fracture toughness ($FT$) was evaluated in both series. As a general trend, there is a decrease in the hardness and Young's modulus with increasing penetration depth. The addition of $Li_2O$ and $TiO_2$ instead of ZnO leads to improved hardness and elastic modulus values. Regarding the $H/E$ ratio, it was found that the samples with lower $TeO_2$ content should be significantly more crack-resistant compared to the higher $TeO_2$ content samples. The $H^3/E^2$ ratio, being lower than 0.01, revealed a poor resistance of these glasses to plastic deformation. At the same time, a decrease of the fracture toughness with increasing $TeO_2$ content was noticed for each glass series. Based on dilatometry measurements, the thermal expansion coefficient as well as the characteristic temperatures of the glasses were measured. Field Emission Scanning Electron Microscopy-Energy Dispersive X-ray analysis (FESEM-EDX) revealed a uniform distribution of the elements in the bulk samples. The mechanical properties of these vitreous materials are important in relation to their application as magneto-optical Faraday rotators in laser cavities.

**Keywords:** mechanical properties; phosphate glass; scanning electron microscopy; tellurite glass; thermal expansion coefficient

## 1. Introduction

Mechanical properties of phosphate glasses and glass ceramics were investigated in relation to their application as solid electrolytes in Na-ion batteries [1]. It was found that glass ceramics obtained by an appropriate heat treatment of the starting glass exhibit an increased microhardness and Young's modulus compared to the vitreous material. Improved mechanical properties of $Na_2O$-$CaO$-$Al_2O_3$-$Ga_2O_3$-$P_2O_5$ (NCAGP) glass with an $Ag^+ \rightarrow Na^+$ ion exchange process were reported [2]. The ion exchanged NCAGP glass is a potential electrolyte material for Na-batteries. The addition of up to 6 mol. % $B_2O_3$ in the phosphate glass content results in an increase of the flexural strength and hardness of the glass as well as a small decrease of the fracture toughness [3]. The electrochemical–mechanical modelling of all-solid-state lithium-ion batteries, including glasses and glass ceramics, has been very recently presented as a promising candidate for next-generation energy storage and sensor applications [4–7].

Increased values of hardness, Young's modulus and fracture toughness of Bi, Pb-doped borophosphate glasses were reported [8] in comparison with the un-doped phosphate glasses [9] and rare-earth-doped phosphate glasses [10], due to the mixed glass former role of $P_2O_5$ and $B_2O_3$ components, which contribute to structural strengthening. The deformation of phosphate glasses under different load (strain) rates depends on the evolution of four mechanisms, namely, elastic deformation, densification, shear flow and fracture [11]. For reduced indentation loads, the first two mechanisms are prevalent, whereas shear flow and fracture are predominant for high-applied loads.

Optical components based on vitreous phosphate materials, such as mirrors, telescopes, lenses, etc., require adequate mechanical strength due to their handling and mounting in optical and optoelectronic devices [12–14]. The mechanical resistance of the phosphate glasses was reported to be improved by noble metal precipitation in the vitreous network, after appropriate heat treatment [15].

Tellurite glasses were investigated for their applications in solid electrolyte batteries [16]. It was found that the embedding of AgI in the glass network reduces the rigidity and the mechanical strength of the vitreous material. Mechanical properties of tellurite glasses have also been investigated for their applications in optoelectronic devices [17–20]. Thus, incorporation of $Ag^+$ ions in the structure of zinc tellurite glasses [17] and lead tellurite glasses [18] enhances the mechanical properties and strengthens the vitreous structure. The increase in the $Er_2O_3$ content in zinc tellurite glasses [19] increases the mechanical strength of these vitreous materials. Elastic properties of $WO_3$-$B_2O_3$-$MgO$-$TeO_2$ and $Ag_2O$-$V_2O_5$-$MoO_3$-$TeO_2$ glasses were also presented in correlation with the mixed former effect of $WO_3$, $MoO_3$, $TeO_2$, and $B_2O_3$ compounds [20].

In this work, results concerning the mechanical properties of some aluminum phosphate-tellurite glass compositions containing ZnO and $Li_2O$-$TiO_2$, respectively, are presented. The hardness, Young's modulus, and fracture toughness of these vitreous materials were investigated in correlation with their composition and structure [21]. The main goal of the paper is related to the study of the structural, mechanical, thermal, and morphological properties of phosphate-tellurite glasses, taking into consideration their potential application for magneto-optical Faraday rotators.

## 2. Materials and Methods

ZnO and $Li_2O$-$TiO_2$-containing phosphate glasses studied in this work belong to the oxide systems $(50-x)ZnO$-$10Al_2O_3$-$40P_2O_5$-$xTeO_2$ ($x$ = 5, 10) (henceforth named as Series A glasses) and $(40-x)Li_2O$-$10Al_2O_3$-$5TiO_2$-$45P_2O_5$-$xTeO_2$ ($x$ = 5, 10) (henceforth named as Series B glasses), respectively. These vitreous materials were synthesized by a non-conventional wet-route of starting reagents that involves the incorporation of the starting analytical purity solid reagents (ZnO, $Li_2CO_3$, $Al_2O_3$, $TiO_2$, $TeO_2$) into an 85% $H_3PO_4$ aqueous solution followed by evaporation by heating at 150 °C, under constant mechanical stirring. The steps of the experimental procedure were: (1) homogenization-evaporation of the

batch; (2) melt-quenching of the batch; (iii) glass annealing; and (iv) optical processing of glasses. All the chemical reagents were purchased from Sigma-Aldrich. The benefits of the wet non-conventional technique are reported in several works of the authors [21–24] that show the role of this method in increasing the chemical and optical homogeneity of the final glasses, taking into consideration the molecular level mixing of the solid reagents in $H_3PO_4$ aqueous solution. In Table 1, the preliminary heat treatment and melting–annealing parameters of the prepared glasses are shown.

**Table 1.** Preliminary heat treatment and melting–annealing parameters of the prepared glasses ($T_g$ is the vitreous transition temperature determined from the thermal expansion curves measured in the 20–500 °C range, not presented in this work).

| Glass Code | Molar Composition | Preliminary Heat Treatment Parameters | Melting and Refining Parameters | Annealing Parameters | Glass Aspect |
|---|---|---|---|---|---|
| A1 | 45ZnO 10Al$_2$O$_3$ 40P$_2$O$_5$ 5TeO$_2$ | Homogenization & evaporation at 200 °C, for 1 h, followed by heat treatment at 700 °C, for 7 h | Melting at 1100 °C, for 30 min, followed by refining at 1125 °C, for 30 min | Plateau at 390 °C, for 30 min, followed by gradually quenching ($T_g$ = 404 °C) | Transparent mauve reddish color |
| A2 | 40ZnO 10Al$_2$O$_3$ 40P$_2$O$_5$ 10TeO$_2$ | Homogenization & evaporation at 200 °C, for 0.5 h, followed by heat treatment at 700 °C, for 2.5 h | Melting at 1100 °C, for 30 min, followed by refining at 1125 °C, for 30 min | Plateau at 400 °C, for 30 min, followed by gradually quenching ($T_g$ = 429 °C) | Transparent dark reddish color |
| B1 | 35Li$_2$O 10Al$_2$O$_3$ 5TiO$_2$ 45P$_2$O$_5$ 5TeO$_2$ | Homogenization & evaporation at 200 °C, for 25 min, followed by heat treatment at 700 °C, for 2.5 h | Melting at 1225 °C, 30 min, followed by refining at 1250 °C, for 30 min | Plateau at 420 °C, for 0.5 h, followed by gradually quenching ($T_g$ = 419 °C) | Transparent dark reddish—brown color |
| B2 | 30Li$_2$O 10Al$_2$O$_3$ 5TiO$_2$ 45P$_2$O$_5$ 10TeO$_2$ | Homogenization & evaporation at 200 °C, for 60 min, followed by heat treatment at 240 °C, for 2 h, and 700 °C, for 3 h | Melting at 1200 °C, for 30 min, followed by refining at 1225 °C, for 30 min | Plateau at 400 °C, for 30 min, followed by gradually quenching ($T_g$ = 427 °C) | Transparent dark brown color |

The homogenization of the glass batches was performed by using an alumina stirrer (Morgan, Fairfield, NJ, USA) at an average rate of 200 rot/min in alumina crucibles (SEPA-DIN, Romania) in order to improve the optical homogeneity of the final materials by the reduction of the gaseous inclusions and embedded striae. The casting of the glass melt occurred in preheated graphite molds followed by subsequent annealing to remove the remnant stress from the final product.

The X-ray diffraction (XRD) measurements were performed at room temperature, in the 10° to 80° range, with a 0.05° step and 3 s integration time, using a Bruker D8 Advance device (Bruker, Billerica, MA, USA) (CuK$\alpha$, $\lambda$ = 1.54056 Å).

For the mechanical characterization stages, the glass samples were embedded in low contraction resin, followed by polishing up to a mirror-like finish.

The hardness (*H*), elastic modulus (*E*), and fracture toughness (*FT*) were assessed by instrumented indentation using an NHT² indenter from CSM Instruments/Anton Paar (Peseux, Switzerland) equipped with a diamond Berkovich geometry three-sided pyramidal tip. Prior to the measurement stage, tip calibration was performed using a fused silica caliber to overcome the effect of tip rounding. Sets of 5 indentations per load, up to the desired value, were performed on each glass sample (10 mN, 50 mN, 100 mN, 200 mN, and 400 mN maximum loads) in different areas. The indentation protocol was: approach speed 2000 nm/min, 30 s loading stage, 3 s dwell time (to minimize the creep effect), and

10 s unloading stage. The loading–unloading curves were processed using the Oliver–Pharr method [25,26].

In order to determine the fracture toughness (*FT*) of brittle materials using indentation tests, several models have been advanced over the last few decades [27–32]. The *FT* parameter was calculated for each glass sample using the model proposed in [32,33], based on the *H* and *E* values determined from indentation tests, the lengths of the cracks from the corners of the imprints, and the applied maximum load. Thus, sets of 6 nanoindentation tests were performed on each glass sample in different areas, with a maximum load of 500 mN, while keeping the remaining parameters identical to the previous measurements. The length of the cracks was assessed by optical microscopy, and the results were averaged.

The thermal expansion coefficient was determined by the dilatometry method using a horizontal Netzsch-Gerätebau DIL 400 PC device (Germany). The temperature was increased by 3 °C/min. The characteristic temperatures (strain point, $T_S$, glass transition temperature, $T_g$, annealing point, $T_A$, and softening point, $T_D$), as well as the thermal expansion coefficient ($\alpha_{20}^{300}$) of the glass, were assessed by processing the results from the dilatometry measurements. The measurement errors for the thermal expansion coefficient were in the range $\pm 0.8 \times 10^{-7}$ K$^{-1}$, provided by calibration with a SiO$_2$ standard sample, according to ISO 7991.

The morphology and the elemental composition of the phosphate-tellurite glasses were evaluated using a Gemini 500 Carl Zeiss field emission scanning electron microscope (FESEM) (Carl Zeiss, Oberkochen, Germany) equipped with a Bruker QUANTAX 200 Energy Dispersive X-ray Spectrometer (EDX) (Brucker, Bremen, Germany), with an XFlash 6 silicon drift detector, energy resolution < 129 eV at Mn-Ka, and Peltier cooling. FESEM images at good resolution were acquired without covering the samples with metallic gold.

## 3. Results and Discussions

### 3.1. X-ray Diffraction

The X-ray diffraction pattern of A1, A2, B1, and B2 glasses were collected at room temperature and are shown in Figure 1. The graphs corroborate the amorphous nature of the explored materials.
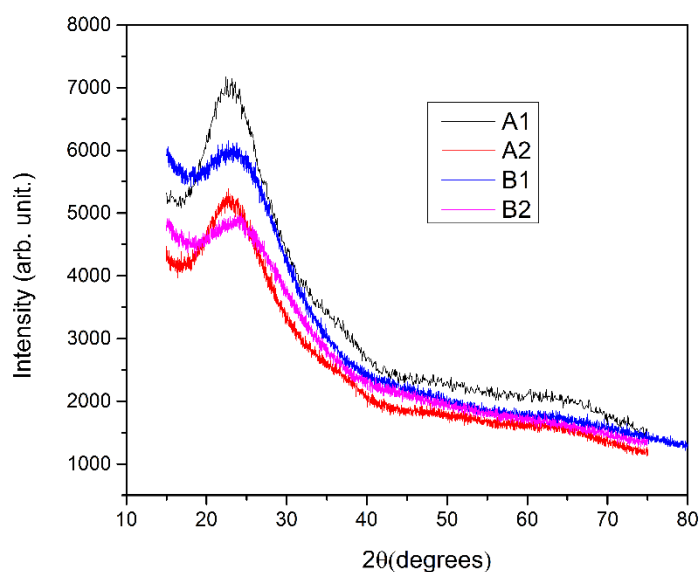


**Figure 1.** XRD patterns of A1, A2, B1, and B2 glasses.

### 3.2. Hardness and Elastic Modulus

The penetration depth *(PD)*, as a result of the indentation tests for the applied loads (10 mN, 50 mN, 100 mN, 200 mN, and 400 mN) on each glass, is influenced by the chemical composition of the investigated vitreous materials.

Table 2 presents the average values for *H*, *E*, and the *H/E* and $H^3/E^2$ ratios, all as a function of the applied load and, consequently, as a function of *PD*. At the subsurface level, series A samples exhibit poorer mechanical behavior, compared to series B samples. This phenomenon would signify that the addition of $Li_2O$ and $TiO_2$, instead of ZnO, leads to enhanced *H* and *E* values. This observation is better visualized in the graph from Figure 2, where one can observe the variation of *H* (a) and *E* (b), as function of the *PD*, for all the samples presented herein.

**Table 2.** Average values of *H*, *E*, *H/E*, and $H^3/E^2$ ratios.

| Glass Code | A1 | | | | A2 | | | | B1 | | | | B2 | | | |
|---|---|---|---|---|---|---|---|---|---|---|---|---|---|---|---|---|
| Load | *H* | *E* | *H/E* | $H^3/E^2$ | *H* | *E* | *H/E* | $H^3/E^2$ | *H* | *E* | *H/E* | $H^3/E^2$ | *H* | *E* | *H/E* | $H^3/E^2$ |
| 10 mN | 4.22 | 52.49 | 0.080 | 0.027 | 4.25 | 58.94 | 0.072 | 0.022 | 6.28 | 71.19 | 0.088 | 0.049 | 6.16 | 77.51 | 0.080 | 0.039 |
| 50 mN | 4.06 | 45.81 | 0.089 | 0.032 | 4.47 | 54.70 | 0.082 | 0.030 | 5.95 | 61.67 | 0.096 | 0.055 | 6.28 | 71.41 | 0.088 | 0.049 |
| 100 mN | 3.82 | 41.71 | 0.092 | 0.032 | 4.35 | 53.14 | 0.082 | 0.029 | 5.70 | 57.02 | 0.100 | 0.057 | 6.14 | 68.26 | 0.090 | 0.050 |
| 200 mN | 3.69 | 37.05 | 0.100 | 0.037 | 4.28 | 50.32 | 0.085 | 0.031 | 5.28 | 49.80 | 0.106 | 0.059 | 5.68 | 64.53 | 0.088 | 0.044 |
| 400 mN | 3.40 | 31.26 | 0.109 | 0.040 | 4.18 | 47.05 | 0.089 | 0.033 | 4.46 | 41.07 | 0.109 | 0.053 | 4.86 | 57.31 | 0.085 | 0.035 |
| 500 mN | 3.45 | 29.97 | 0.115 | 0.046 | 4.15 | 45.65 | 0.091 | 0.034 | 4.96 | 40.82 | 0.122 | 0.073 | 5.66 | 59.49 | 0.095 | 0.051 |
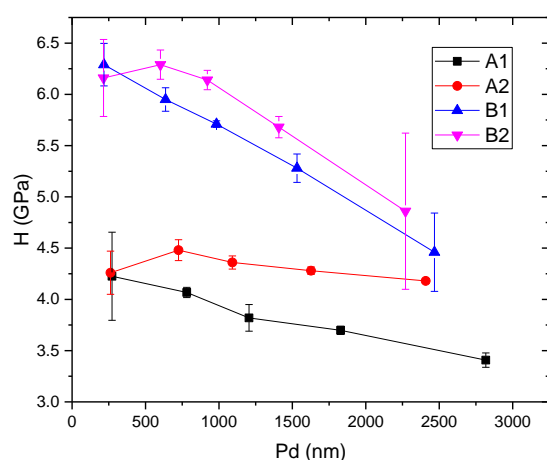


(**a**)
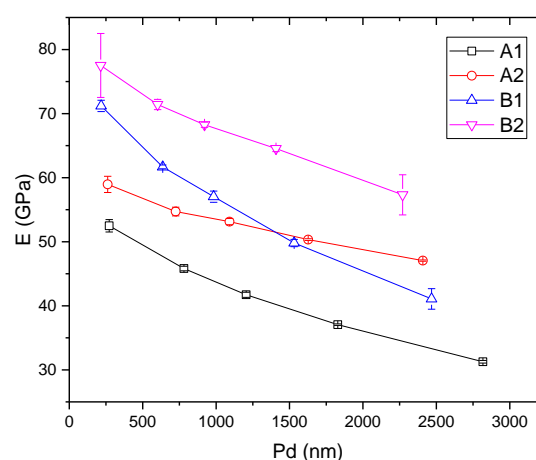
(**b**)

**Figure 2.** The variation of hardness (*H*) (**a**) and indentation elastic modulus (*E*) (**b**), as a function of penetration depth *(PD)*.

As a general trend, one can notice a decrease of *H* and *E* values with increasing penetration depth. In the case of ZnO-containing glasses (Series A), *H* and *E* have higher values when the content of $TeO_2$ increases and ZnO content decreases. In the case of $Li_2O$-$TiO_2$-containing glasses (Series B), the increase in $TeO_2$ content does not significantly influence the hardness; however, the difference in the variation of the elastic modulus is more obvious, with sample B2 exhibiting higher values for this parameter. The substitution of ZnO by $Li_2O$-$TiO_2$ for the same $TeO_2$ content (sample B2 compared to sample A2) results in a significant increase in the mechanical parameter values. ZnO is generally used to improve the glass quality because it contributes to an increase of the chemical stability and durability [34–36] as well as high *E* values [37]. Our findings show that the addition

of ZnO cannot be considered a foolproof solution to improve the mechanical characteristics of such glasses. It was shown elsewhere that gradual replacement of $TeO_2$ with $Li_2O$ in the $(70-x)TeO_2 + 15B_2O_3 + 15P_2O_5 + xLi_2O$ ($x$ = 5, 10, 15, 20, 25, 30 mol. %) glass system leads to the decrease of the average crosslink density and rigidity of the prepared samples, which affects the mechanical properties (i.e., *H* and *E* values are decreased) [38]. In the case of the explored phosphate-tellurite glasses from this work, the *E* values of $Li_2O$-$TiO_2$-containing glasses are higher than those of ZnO-containing glasses for the same $TeO_2$ content. As a conclusion, it can be stated that the increase in $TeO_2$ content, as well as the replacement of ZnO by $Li_2O$-$TiO_2$, determines an increase in *H* and *E* values. This is in agreement with [39], where it was shown that the addition of $TiO_2$ in $(95-x)TeO_2$-$5La_2O_3$-$xTiO_2$, ($x$ = 0–20 mol. %) glasses caused an increase of *H* and *E* values. This is due to the formation of Ti-O-Ti bonds that caused an increase in stability and stiffness of the glasses. The same effect of $TiO_2$ addition to the increasing of *E* values and glass durability was found for bioactive phosphate glasses reported in [40,41]. Some reference values of *H* and *E* for different phosphate glasses are presented elsewhere [9].

Apart from hardness, it is clear that Young's modulus has a crucial role in the mechanical behavior of a material. The *H*/*E* ratio, called elastic strain to failure, can be a suitable parameter with the ability to predict, to a certain extent, the wear resistance of materials. Materials with high *H*/*E* ratio values generally exhibit better wear and failure resistance. This ratio can be used to predict whether the material will crack or not under load. Materials with high hardness and relatively lower values of Young's modulus should exhibit improved fracture toughness. Materials with a high *H*/*E* ratio have a high plasticity index, meaning that their deformation under load is more likely to be elastic than plastic. Consequently, it is desirable to obtain a large *H*/*E* value, meaning sufficiently high hardness (to resist plastic deformation), but with a low elastic modulus. According to previous studies, materials with *H*/*E* ≥ 0.1 are considered to be resistant to cracking [41,42].

Furthermore, the $H^3/E^2$ ratio is a strong indicator of the resistance of a material to plastic deformation, a ranking parameter for prediction of shear banding under localized deformation. The $H^3/E^2$ ratio is not generally used to assess the wear and failure resistance of a material; however, it gives an estimation regarding its elasticity [43]. Materials with $H^3/E^2$ ≥ 0.1 are estimated to be resistant to plastic deformation.

The variation of these two ratios, based on the *H* and *E* values obtained through instrumented indentation, as a function of penetration depth is presented in Figure 3. One can observe that if the previously mentioned predictions are accurate, the samples with lower $TeO_2$ content should be significantly more resistant to cracking compared to the remaining samples.

As far as the $H^3/E^2$ ratio is concerned, considering that the maximum value exhibited by the samples presented herein is below 0.06, these glasses would exhibit poor resistance to plastic deformation.

Figure 4 represents the loading–unloading curves obtained on these glasses, with an applied load of 500 mN. It is obvious from the lower penetration depth values for the same applied load that the samples from series B are harder, as shown in the previous paragraphs. Furthermore, a particular phenomenon can be inferred from the loading section of these curves, shown in Figure 4b (magnified). Sudden increases in the *PD* values, such as those observed for samples B1 and B2, can signify several events happening in the material: micro-cracks, phase transformations, dislocations, nucleation, and strain transfer across grain boundaries, all due to the applied load. Knowing that the materials in question are amorphous, these sudden increases in *PD* values can be accurately linked with the occurrence of cracks in the material. Consequently, the *FT* analysis, based on the occurrence of these cracks, will be presented in the next subsection.
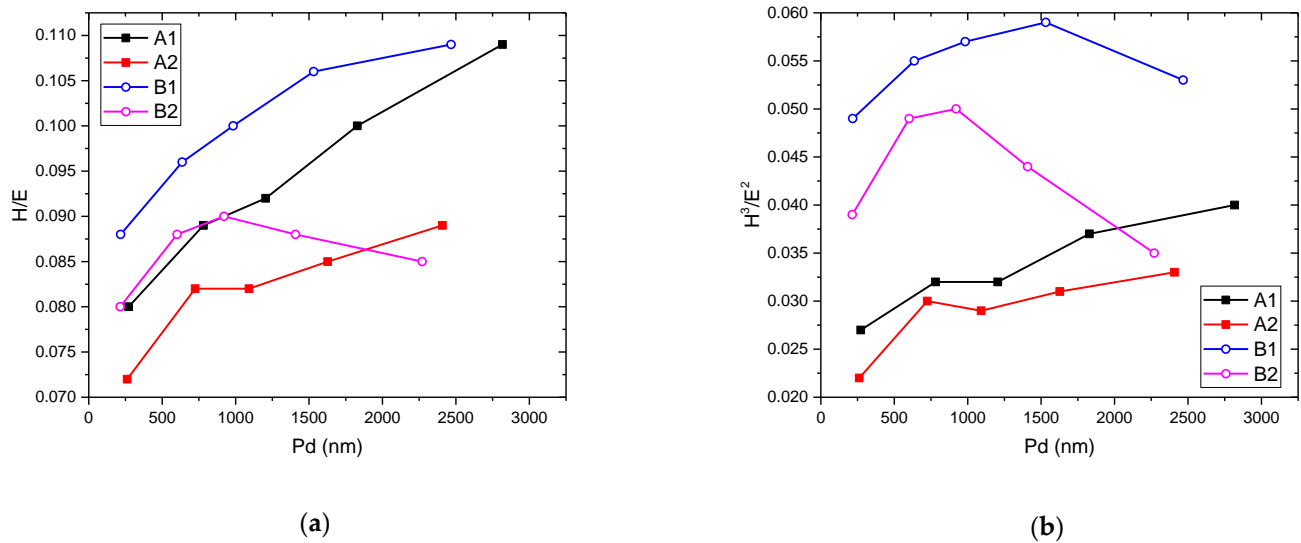
(**a**)



(**b**)

**Figure 3.** The variation of *H/E* (**a**) and $H^3/E^2$ (**b**) ratios, as a function of the penetration depth.
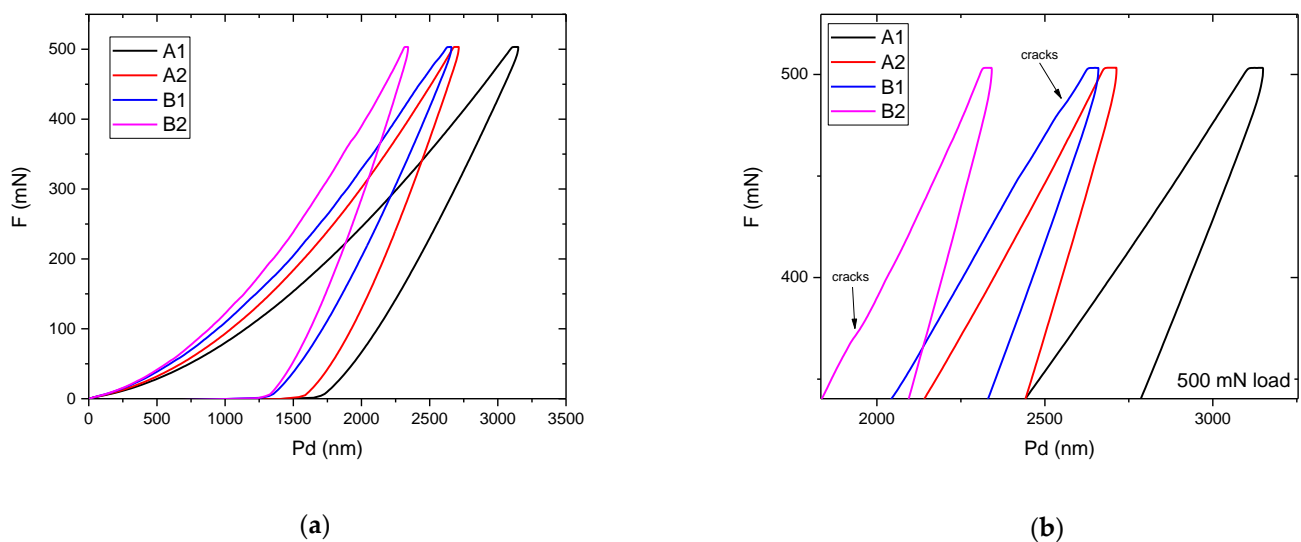


(**a**)



(**b**)

**Figure 4.** The loading—unloading curves obtained using 500 mN load (**a**); detail of the same curves, showing small deviations which signify the occurrence of cracks (**b**).

### 3.3. Fracture Toughness

Figure 5 shows schematically the geometrical characteristics needed for calculating the *FT* values, based on Berkovich imprints obtained with 500 mN loads. The propagation of radial cracks from the corners of the imprint to the outside, in the bulk material, is of particular interest. Three parameters are important: (i) length *a*, measured from the center of contact to the end of the crack corner; (ii) the crack length *l*, measured from the corner of each imprint; and (iii) length *c*, which is the total length, *a + l*. The asymmetric shape of the Berkovich indenter type does not allow the cracks to join two corners of the imprint by passing through the center of the indentation. Therefore, the formation of radial cracks is more likely to occur. Six nanoindentation tests with an applied load of 500 mN were performed. The averaged values for *a*, *c*, and *l*, and the calculated *FT* parameter ($K_c$), are presented in Table 3.

**Table 3.** Crack parameters (*a*, *l* and *c*) and *Kc*.

| Glass Code | $a$ (m) $\times 10^{-8}$ | $l$ (m) $\times 10^{-8}$ | $c$ (m) $\times 10^{-8}$ | $K_c$ (MPa m$^{1/2}$) |
|:---:|:---:|:---:|:---:|:---:|
| A1 | 1000 | 693 | 1693 | 0.594 |
| A2 | 1018 | 840 | 1858 | 0.554 |
| B1 | 894 | 920 | 1814 | 0.424 |
| B2 | 879 | 1055 | 1934 | 0.420 |

The crack parameters *a*, *l*, and *c*, were used to calculate the *FT* parameter Equation (1), taking into account the average values of *H*, *E*, *PD*, and applied load.
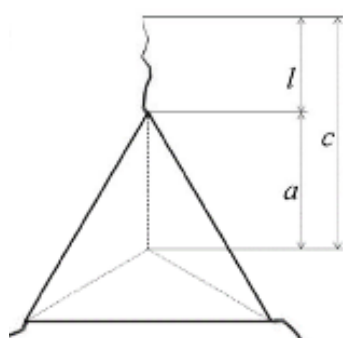


**Figure 5.** Indentation-induced crack geometry for Berkovich tips.

Dukino and Swain [30] changed the method proposed in [31] with a correction factor, initially proposed in [32], to adjust the analysis of cracks induced by Berkovich tip geometry, as shown in Equation (1):

$$K_c = 1.073 x_v \, (a/l)^{1/2} (E/H)^{2/3} \ (P/c^{3/2})$$

(1)

where $x_v = 0.015$ is an empirical calibration constant, *a*, *l*, and *c* are the crack length (m) parameters (see Figure 5), *E* is Young's modulus (Pa), *H* is the hardness (Pa), and *P* is the applied load (N). It was noticed that the $(P/c^{3/2})$ ratio is almost constant and dependent on the material properties [28]. From Table 3, in the case of ZnO-containing glasses, a decrease of *FT* parameter with increasing $TeO_2$ content is noticed. The same trend is noticed in the case of $Li_2O$-$TiO_2$-containing glasses with increasing $TeO_2$ content. A more evident decrease is observed when ZnO is replaced by $Li_2O$-$TiO_2$ for a constant $TeO_2$ content. Some reference values related to the *FT* parameter for different phosphate glasses are presented elsewhere [9].

*3.4. Dilatometry Measurements*

The characteristic temperatures as well as the thermal expansion coefficient values for the glasses from the A and B series are presented in Table 4. The thermal expansion coefficient parameter was determined by the dilatometry method in the 20–300 °C range and it expresses the ratio between elongation and the initial length of the sample.

**Table 4.** Characteristic temperatures and thermal expansion coefficient for A and B glass series.

| Property/Glass Code | A1 | A2 | B1 | B2 |
|:---:|:---:|:---:|:---:|:---:|
| Strain point, $T_s$ | 403 | 403 | 391 | 394 |
| Glass transition temperature, $T_g$ | 426 | 429 | 419 | 427 |
| Annealing point, $T_A$ | 441 | 437 | 426 | 436 |
| Softening point, $T_D$ | 448 | 453 | 439 | 446 |
| Thermal expansion coefficient, $\propto_{20}^{300}$ $\times 10^{-6}$ (K$^{-1}$) | 6.86 | 6.56 | 11.67 | 11.95 |

Taking into consideration the nominal molar formula of the synthesized glass samples, it is possible to state that the vitreous network is built by metaphosphate chains and crosslinked metaphosphate chains formed by P-O-P, P-O-Te and Te-O-Te bonds, revealing the vitreous network-forming role of $P_2O_5$ and $TeO_2$ [21,44].

B series glasses exhibit thermal expansion coefficient values higher than those of the A series, which could be explained by the formation of a less rigid network, characterized by lower energy bonds values and, consequently, lower characteristic temperatures, strain point, $T_S$, glass transition temperature, $T_g$, annealing point, $T_A$, and softening point, $T_D$ (see Table 4). The reason is the presence of $Li_2O$ and $TiO_2$, whose role is to modify the vitreous network, breaking the metaphosphate chains and resulting in non-bridging oxygen atoms, $O^-$ linked by $Li^+$ and $Ti^{4+}$ cations. The energy of the bonds, in this case, is lower than in the case of bridging oxygen atoms P-O-P, P-O-Te, and Te-O-Te, causing a decrease of the network stiffness and higher values of the hardness and elastic modulus as compared to the A glass series. This can explain a reduced remnant deformation, showing in evidence a more pronounced elastic behavior in relation to the A glass series (see Figure 4).

In the case of the A glass series, ZnO in a high amount takes the role of vitreous network former by creating Zn-O-P and Zn-O-Te bonds, consolidating the connections within the phosphate chains and the three-dimensional structures. This can clarify the reduced values of hardness and elastic modulus and higher thermal strength compared to the B glass series. Finally, the less rigid structure and the binding energies with lower values in the case of the B glass series could also elucidate the lower values of the crack resistance coefficients compared to those of the A glass series.

### 3.5. FESEM-EDX Measurements

The samples were analyzed in several zones in order to acquire elemental maps showing in evidence the nano-clustering of diatomic tellurium molecules [45]. The elemental mapping did not reveal these nanoaggregates, tellurium atoms being relatively evenly distributed in the bulk samples.

Figure 6 exhibits the morphology of the glass samples, obtained by FESEM, while Figure 7 shows the elemental maps of the A1, A2, B1, and B2 glass samples.
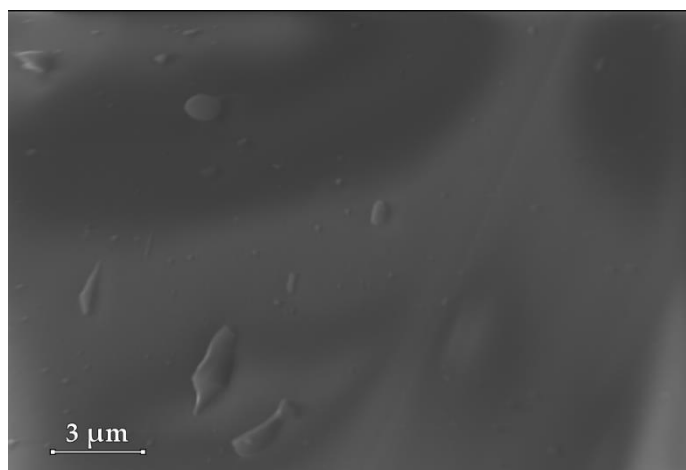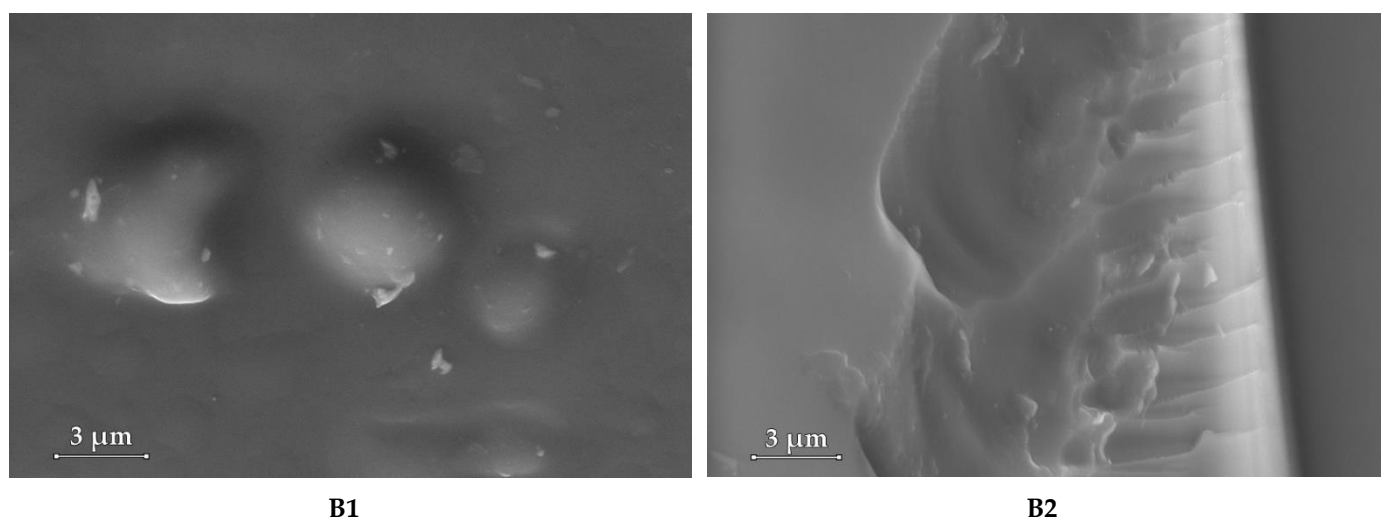


A1
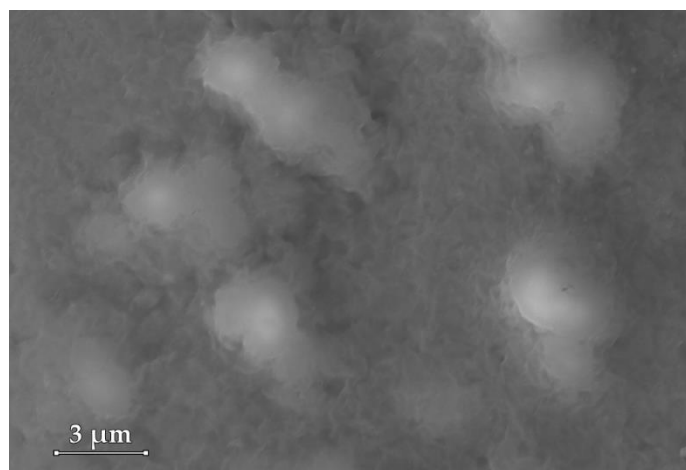


A2

**Figure 6.** Surface morphology of the **A1**, **A2**, **B1**, and **B2** glass samples.
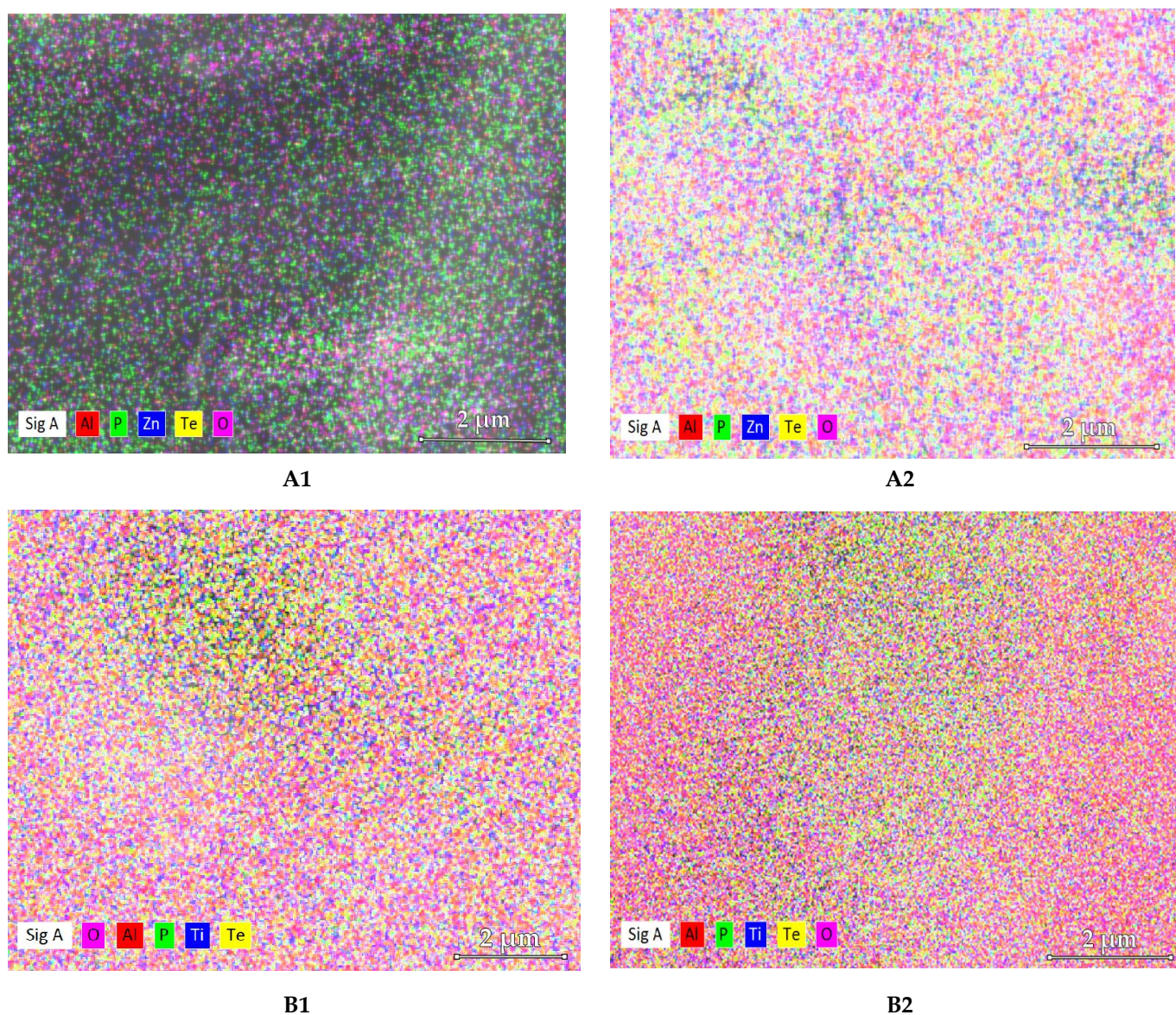


**Figure 7.** Elemental maps of the **A1**, **A2**, **B1**, and **B2** glass samples.

Figure 7 reveals the distribution of the elements (Zn, Al, P, O, Te, and Ti) regarding their dispersion and concentration in the analyzed samples.

Table 5 displays the comparison between the wt. % nominal elemental composition and the composition obtained from EDS for the A1, A2, B1, and B2 glasses.

Lithium could not be detected by EDX due to the low atomic weight, the emission of light elements not being analyzed using this technique. Thus, the EDX elemental composition of B1 and B2 samples presented in Table 5 was calculated considering the lithium percentage in the prepared samples equal to the nominal percentage, and the elemental composition provided by the EDX algorithm for the other elements was normalized by taking into account the lithium percentage.

Although the FESEM images evidenced the presence of small formations in all the evaluated glasses, when analyzing the dispersion and the concentration of the elements in the samples by using EDX elemental mapping, a uniform distribution of the elements was observed. From Table 5, it is observed that, mainly in the case of A2, B1, and B2 glasses, close values of the nominal elemental composition and EDX elemental composition were found.

**Table 5.** Nominal elemental composition and EDX elemental composition of A1, A2, B1, and B2 glasses.

| Glass Sample | Element | Nominal Elemental Composition (wt. %) | EDX Elemental Composition (wt. %) |
|---|---|---|---|
| A1 | Al | 4.85 | 4.27 |
|  | P | 22.25 | 14.05 |
|  | Zn | 26.24 | 5.57 |
|  | Te | 5.74 | 3.26 |
|  | O | 40.92 | 72.85 |
| Total |  | 100.00 | 100.00 |
| A2 | O | 40.21 | 49.82 |
|  | Al | 4.68 | 3.53 |
|  | P | 21.49 | 22.41 |
|  | Te | 11.09 | 6.8 |
|  | Zn | 22.53 | 17.44 |
| Total |  | 100.00 | 100.00 |
| B1 | Li | 5.07 | 5.07 |
|  | O | 51.35 | 56.32 |
|  | Al | 5.59 | 4.46 |
|  | P | 28.88 | 26.39 |
|  | Ti | 2.48 | 2.89 |
|  | Te | 6.63 | 4.87 |
| Total |  | 100.00 | 100.00 |
| B2 | Li | 4.07 | 4.07 |
|  | O | 48.88 | 46.33 |
|  | Al | 5.24 | 6.89 |
|  | P | 27.06 | 30.64 |
|  | Ti | 2.33 | 2.39 |
|  | Te | 12.42 | 9.68 |
| Total |  | 100.00 | 100.00 |

## 4. Conclusions

In the case of ZnO-containing glasses, corresponding to the A glass series ($(50-x)$ZnO-10Al$_2$O$_3$-40P$_2$O$_5$-$x$TeO$_2$ ($x$ = 5, 10)), the hardness increases with TeO$_2$ content, whereas in the case of Li$_2$O-TiO$_2$-containing glasses, corresponding to the B glass series ($(40-x)$Li$_2$O-10Al$_2$O$_3$-5TiO$_2$-45P$_2$O$_5$-$x$TeO$_2$ ($x$ = 5, 10)), the increase in TeO$_2$ content does not considerably influence the hardness of the glasses. The hardness of Li$_2$O-TiO$_2$-containing glasses is higher than that of ZnO-containing glasses for the same TeO$_2$ content. Young's modulus, in the case of ZnO-containing glasses, increases with TeO$_2$ content, the same trend being remarked in the case of Li$_2$O-TiO$_2$-containing glasses. Young's modulus of TiO$_2$-containing glasses is higher than that of ZnO-containing glasses for the same TeO$_2$ content. It can be stated that the increase in TeO$_2$ content, as well as the replacement of ZnO by Li$_2$O-TiO$_2$, determines an increase of the hardness and Young's modulus.

In the case of ZnO-containing glasses, the increase of TeO$_2$ content results in a decrease of fracture toughness (*FT* parameter). The same trend is noticed in the case of Li$_2$O-TiO$_2$-containing glasses with increasing TeO$_2$ content. A more evident decrease of *FT* is observed when ZnO is replaced by Li$_2$O-TiO$_2$ for a constant TeO$_2$ content.

The thermal expansion coefficient values in the case of the B glass series are higher than those of the A glass series due to the less rigid network. Consequently, the characteristic temperatures in the case of the B glass series are lower than those of the A glass series. The presence of different vitreous network modifiers could be the source of the higher hardness and elastic modulus values in the case of the B glass series as compared to those of the A glass series.

FESEM images and EDX elemental maps evidenced a relatively uniform distribution of the constituent elements in the structure of the bulk glasses, ruling out the variation in mechanical behavior due to potential inhomogeneities in the samples.

The correlation between the presence of different vitreous network modifiers and the mechanical properties of the investigated glasses is essential for their application as magneto-optical Faraday rotators.

Future work will be developed related to research of phosphate-tellurite glasses containing post transition and heavy metal ions with magnetic and magneto-optical properties for Faraday rotators.

# References

1. Jha, P.K.; Pandey, O.P.; Singh, K. FTIR spectral analysis and mechanical properties of sodium phosphate glass–ceramics. *J. Mol. Struct.* **2015**, *1083*, 278–285. https://doi.org/10.1016/j.molstruc.2014.11.027.

2. Allu, A.R.; Balaji, S.; Annapurna, K. Electrical and mechanical properties of $Na_{2.8}Ca_{0.1}Al_2Ga_{0.5}P_2O_{12}$ glass based electrolyte materials: Influence of $Ag^+$ ion-exchange. *J. Non-Cryst. Solids* **2018**, *498*, 323–330. https://doi.org/10.1016/j.jnoncrysol.2018.03.043.

3. Zhao, Y.; Zhou, Y.; Yang, J.; Li, Y.; Cheng, L.; Wang, K.; Sun, X.; Sun, C.; Qin, Z. Optimized structural and mechanical properties of borophosphate glass. *Ceram. Int.* **2020**, *46*, 9025–9029. https://doi.org/10.1016/j.ceramint.2019.12.150.

4. Ke, X.; Wang, Y.; Ren, G.; Yuan, C. Towards rational mechanical design of inorganic solid electrolytes for all-solid-state lithium ion batteries. *Energy Storage Mater.* **2020**, *26*, 313–324. https://doi.org/10.1016/j.ensm.2019.08.029.

5. Ataalla, M.; Afify Ahmed, S.; Hassan, M.; Adam, A.M.; Milanova, M.; Piroeva, I. Humidity Sensing Properties of Tungsten Based Glass Crystalline Materials in the $WO_3$-ZnO-$La_2O_3$-$Al_2O_3$ System. In *Advanced Nanotechnologies for Detection and Defence against CBRN Agents-Part of NAPSB*; Springer: Dordrecht, The Netherlands, 2018; pp. 417–425. https://doi.org/10.1007/978-94-024-1298-7.

6. Boora, M.; Malik, S.; Kumar, V.; Bala, M.; Arora, S.; Rohilla, S.; Kumar, A.; Dalal, J. Investigation of structural and impedance spectroscopic properties of borate glasses with high $Li^+$ concentration. *Solid State Ion.* **2021**, *368*, 115704. https://doi.org/10.1016/j.ssi.2021.115704.

7. Tijaria, M.; Sharma, Y.; Kumar, V.; Dahiya, S.; Dalal, J. Effect of $Na_2O$ on physical, structural and electrical properties of borate glasses. *Matter. Today Proceed.* **2021**, *45*, 3722–3725. https://doi.org/10.1016/j.matpr.2020.12.688.

8. Sava, B.A.; Boroica, L.; Elisa, M.; Shikimaka, O.; Grabco, D.; Popa, M.; Barbos, Z.; Iordanescu, R.; Niculescu, A.M.; Kuncser, V.; et al. Bismuth and lead oxides codoped boron phosphate glasses for Faraday rotators. *Ceram. Int.* **2018**, *44*, 6016–6025. https://doi.org/10.1016/j.ceramint.2017.12.205.

9. Sglavo, V.M.; Mura, E.; Milanese, D.; Lousteau, J. Mechanical properties of phosphate glass optical fibers. *Int. J. Appl. Glass Sci.* **2014**, *5*, 57–64. https://doi.org/10.1111/ijag.12040.

10. Grabco, D.Z.; Shikimaka, O.A.; Elisa, M.; Sava, B.A.; Boroica, L.; Pyrtsak, C.; Prisacaru, A.; Danitsa, Z.; Feraru, I.; Ursu, D. Features of the mechanical properties of phosphate glasses doped with rare earth elements under indentation. *Surf. Eng. Appl. Electrochem.* **2012**, *48*, 365–374. https://doi.org/10.3103/S1068375512040072.

11. Shikimaka, O.; Grabco, D.; Sava, B.A.; Elisa, M.; Boroica, L.; Harea, E.; Pyrtsac, C.; Prisacaru, A.; Barbos, Z. Densification contribution as a function of strain rate under indentation of terbium-doped aluminophosphate glass. *J. Mater. Sci.* **2016**, *51*, 1409–1417. https://doi.org/10.1007/s10853-015-9460-8.

12. Mukherjee, D.P.; Das, S.K. The influence of $TiO_2$ content on the properties of glass ceramics: Crystallization, microstructure and hardness. *Ceram. Int.* **2014**, *40*, 4127–4134. https://doi.org/10.1016/j.ceramint.2013.08.067.

13. Zhou, Y.; Zheng, H.; Zhao, S.; Zhang, C.; Bai, W.; Sun, C.; Tong, Y.; Yang, J. Preparation, structural and mechanical characterization of ceria-added phosphate glasses. *J. Non-Cryst. Solids* **2021**, *570*, 120878. https://doi.org/10.1016/j.jnoncrysol.2021.120878.

14. Zhang, W.; Yu, J.; Cai, Y.; Jiang, G.; Huang, W.; Ji, F. Abrasion performance of phosphate laser glass in dry and humid air. *J. Chin. Ceram. Soc.* **2015**, *43*, 1008–1016. https://doi.org/10.14062/j.issn.0454-5648.2015.07.26.

15. Rao, G.V.; Shashikala, H.D. Optical, dielectric and mechanical properties of silver nanoparticle embedded calcium phosphate glass. *J. Non-Cryst. Solids* **2014**, *402*, 204–209. https://doi.org/10.1016/j.jnoncrysol.2014.06.007.

16. Halimah, M.K.; Daud, W.M.; Sidek, H.A.A. Effect of AgI addition on elastic properties of quaternary tellurite glass systems. *Chalcogenide Lett.* **2010**, *7*, 613–620.

17. Tafida, R.A.; Halimah, M.K.; Muhammad, F.D.; Chan, K.T.; Onimisi, M.Y.; Usman, A.; Hamzad, A.M.; Umar, S.A. Structural, optical and elastic properties of silver oxide incorporated zinc tellurite glass system doped with Sm3+ ions. *Mater. Chem. Phys.* **2020**, *246*, 122801. https://doi.org/10.1016/j.matchemphys.2020.122801.

18. Culea, E.N.; Pascut, P.; Pustan, M.; Tamas-Gavrea, D.R.; Pop, L.; Vida-Simiti, I. Effects of Eu:Ag codoping on structural, magnetic and mechanical properties of lead tellurite glass ceramics. *J. Non-Cryst. Solids* **2015**, *408*, 18–25. https://doi.org/10.1016/j.jnoncrysol.2014.10.002.

19. Nazrin, S.N.; Halimah, M.K.; Muhammad, F.D.; Yip, J.S.; Hasnimulyati, L.; Fazzny, M.F.; Hazlin, M.A.; Zaitizila, I. The effect of erbium oxide in physical and structural properties of zinc tellurite glass system. *J. Non-Cryst. Solids* **2018**, *490*, 35–43. https://doi.org/10.1016/j.jnoncrysol.2018.03.017.

20. El-Moneim, A.A.; El-Mallawany, R. Analysis and prediction for elastic properties of quaternary tellurite $Ag_2O$–$V_2O_5$–$MoO_3$–$TeO_2$ and $WO_3$–$B_2O_3$–MgO–$TeO_2$ glasses. *J. Non-Cryst. Solids* **2019**, *522*, 119580. https://doi.org/10.1016/j.jnoncrysol.2019.119580.

21. Elisa, M.; Boroica, L.; Sava, B.A.; Iordache, S.M.; Iordache, A.-M.; Vasiliu, I.C.; Stefan, R.C.; Galca, A.C.; Kuncser, V.; Eftimie, M. Synthesis and characterization of a titanium phosphate-tellurite glass for Faraday rotators. *J. Am. Ceram. Soc.* **2020**, *103*, 3978–3990. https://doi.org/10.1111/jace.17071.

22. Elisa, M.; Stefan, R.; Vasiliu, I.C.; Rusu, M.I.; Sava, B.A.; Boroica, L.; Sofronie, M.; Kuncser, V.; Galca, A.C.; Beldiceanu, A.; et al. Thermal, structural, magnetic and magneto-optical properties of dysprosium-doped phosphate glass. *J. Non-Cryst. Solids* **2019**, *521*, 119545. https://doi.org/10.1016/j.jnoncrysol.2019.119545.

23. Elisa, M.; Iordanescu, R.; Vasiliu, C.; Sava, B.A.; Boroica, L.; Valeanu, M.; Kuncser, V.; Galca, A.C.; Volceanov, A.; Eftimie, M.; et al. Magnetic and magneto-optical properties of Bi and Pb-containing aluminophosphate glass. *J. Non-Cryst Solids* **2017**, *465*, 55–58. https://doi.org/10.1016/j.jnoncrysol.2016.11.010.

24. Elisa, M.; Vasiliu, I.C.; Sava, B.A.; Boroica, L.; Filip, A.V.; Dinca, M.C.; Bartha, C. Phase and structural characterization of phosphate-tellurite crystalline materials. *J. Optoelectron. Adv. Mater.* **2021**, 23, 257–263.

25. Oliver, W.C.; Pharr, G.M. Measurement of hardness and Young's modulus by instrumented indentation: Advances in understanding and refinements to methodology. *J. Mater. Res.* **2004**, *19*, 3. https://doi.org/10.1557/jmr.2004.19.1.3.

26. Oliver, W.C.; Pharr, G.M. An improved technique for determining hardness and elastic modulus using load and displacement sensing indentation experiments. *J. Mater. Res.* **1992**, *7*, 1564–1583. https://doi.org/10.1557/JMR.1992.1564.

27. Palmqvist, S. A method to determine the toughness of brittle materials, especially hard metals. *Jernkontorets Ann.* **1957**, *141*, 303–307.

28. Lawn, B.R.; Evans, A.G.; Marshall, D.B. Elastic/plastic indentation damage in ceramics: The median/radial crack system. *J. Am. Ceram. Soc.* **1980**, *63*, 574–581. https://doi.org/10.1111/j.1151-2916.1980.tb10768.x.

29. Anstis, G.R.; Chantikul, P.; Lawn, B.R.; Marshall, D.B. A critical evaluation of indentation techniques for measuring fracture toughness: I, Direct crack measurements. *J. Am. Ceram. Soc.* **1981**, *64*, 533–538. https://doi.org/10.1111/j.1151-2916.1981.tb10320.x.

30. Dukino, R.D.; Swain, M.V. Comparative measurement of indentation fracture toughness with Berkovich and Vickers indenters. *J. Am. Ceram. Soc.* **1992**, *75*, 3299–3304. https://doi.org/10.1111/j.1151-2916.1992.tb04425.x.

31. Laugier, M.T. Palmqvist indentation toughness in WC-Co composites. *J. Mater. Sci. Lett.* **1987**, *6*, 897–900. https://doi.org/10.1007/BF01729862.

32. Ouchterlony, F. Stress intensity factors for the expansion loaded star crack. *Eng. Fract. Mech.* **1976**, *8*, 447–448. https://doi.org/10.1016/0013-7944(76)90026-6.

33. Lamuta, C.; Cupolillo, A.; Politano, A.; Aliev, Z.S.; Babanly, M.B.; Chulkov, E.V.; Pagnotta, L. Indentation fracture toughness of single-crystal $Bi_2Te_3$ topological insulators. *Nano Res.* **2016**, *9*, 1032–1042. https://doi.org/10.1007/s12274-016-0995-z.

34. Aboulfotoh, N.; Elbashar, Y.; Ibrahem, M.; Elokr, M. Characterization of copper doped phosphate glasses for optical applications. *Ceram. Int.* **2014**, *40*, 10395–10399. https://doi.org/10.1016/j.ceramint.2014.02.125.

35. Omrani, R.O.; Krimi, S.; Videau, J.J.; Khattech, I.; El Jazouli, A.; Jemal, M. Structural and thermochemical study of $Na_2O$–$ZnO$–$P_2O_5$ glasses. *J. Non-Cryst. Solids* **2014**, *390*, 5–12. https://doi.org/10.1016/j.jnoncrysol.2014.02.020.

36. Matori, K.A.; Sayyed, M.I.; Sidek, H.A.A.; Zaid, M.H.M.; Singh, V.P. Comprehensive study on physical, elastic and shielding properties of lead zinc phosphate glasses. *J. Non-Cryst. Solids* **2017**, *457*, 97–103. https://doi.org/10.1016/j.jnoncrysol.2016.11.029.

37. Matori, K.A.; Zaid, M.H.M.; Quah, H.J.; Aziz, S.H.A.; Wahab, Z.A.; Ghazali, M.S.M. Studying the effect of ZnO on physical and elastic properties of $(ZnO)_x(P_2O_5)_{1-x}$ glasses using nondestructive ultrasonic method. *Adv. Mater. Sci. Eng.* **2015**, *2015*, 596361. https://doi.org/10.1155/2015/596361.

38. Khafagy, A.H.; El-Adawy, A.A.; Higazy, A.A.; El-Rabaie, S.; Eid, A.S. Studies of some mechanical and optical properties of: (70-x)$TeO_2$ + 15$B_2O_3$ + 15$P_2O_5$ + x$Li_2O$ glasses. *J. Non-Cryst. Solids* **2008**, *354*, 3152–3158. https://doi.org/10.1016/j.jnoncrysol.2008.01.013.

39. Sapian, I.N.; Yusof, M.I.M.; Yahya, A.K. Elastic and structural properties of (95-x)$TeO_2$-5$La_2O_3$-x$TiO_2$ lanthanum tellurite glass system. *Chalcogenide Lett.* **2014**, *11*, 471–484.

40. Kiani, A.; Lakhkar, N.J.; Salih, V.; Smith, M.E.; Hanna, J.V.; Newport, R.J.; Pickup, M.; Knowles, J.C. Titanium-containing bioactive phosphate glasses. *Philos. Trans. R. Soc. A* **2012**, *370*, 1352–1375. https://doi.org/10.1098/rsta.2011.0276.

41. Leyland, A.; Matthews, A. On the significance of the H/E ratio in wear control: A nanocomposite coating approach to optimised tribological behavior. *Wear* **2000**, *246*, 1–11. https://doi.org/10.1016/S0043-1648(00)00488-9.

42. Postolnyi, B.O.; Konarski, P.; Komarov, F.F.; Sobol, O.V.; Kyrychenko, O.V.; Shevchuk, D.S. Study of Elemental and Structural Phase Composition of Multilayer Nanostructured TiN / MoN Coatings, their Physical and Mechanical Properties. *J. Nano-Electron. Phys.* **2014**, *6*, 04016.

43. Kolaklieva, L.; Kakanakov, R.; Stefanov, P.; Kovacheva, D.; Atanasova, G.; Russev, S.; Chitanov, V.; Cholakova, T.; Bahchedjiev, C. Mechanical and structural properties of nanocomposite CrAlSiN–AlSiN coating with periodically modulated composition. *Coatings* **2020**, *10*, 41. https://doi.org/10.3390/coatings10010041.

44. Elisa, M.; Stefan, R.C.; Vasiliu, I.C.; Iordache, S.M.; Iordache, A.-M.; Sava, B.A.; Boroica, L.; Dinca, M.C.; Filip, A.V.; Galca, A.C.; et al. A new zinc phosphate-tellurite glass for magneto-optical applications. *Nanomaterials* **2020**, *10*, 1875. https://doi.org/10.3390/nano10091875.

45. Kaky, K.M.; Lakshminarayana, G.; Baki, S.O.; Kityk, I.V.; Taufiq-Yap, Y.H.; Mahdi, M.A. Structural, thermal and optical absorption features of heavy metal oxides doped tellurite rich glasses. *Results Phys.* **2017**, *7*, 166–174. https://doi.org/10.1016/j.rinp.2016.12.013.